directional bias in the diffusion analysis is inconsequential.

Figure 5 displays a series of unequally timed images of 48.5-kbp DNA, the largest of this study. The equilibrium radius of gyration and contour length are 0.73 and 22 μm, respectively (*20*). Fully stretched, this molecule would span more than 20 cavities, seemingly enough to define a reptation tube. Indeed, some aspects of reptation are noted in this molecule's motion. Nevertheless, as indicated in Movie S2 (SOM), most aspects of the motion differ markedly from classic reptation. With a fluctuating number of cavities occupied, motion is more akin to the bunching and stretching of an inchworm. In contrast to the smaller DNA molecules, diffusion can no longer be interpreted in terms of discrete cavity-to-cavity jumps. Although localization to a single cavity still occurs, the dominant configuration is occupation of two adjacent cavities. Figure 5 shows a variety of three- and four-cavity configurations that are both bent and straight. Interestingly, linear molecules spanning three or four cavities rarely form new configurations through "hernias" that spill out laterally from central cavities. Instead, the molecules dominantly alter configuration by expanding or contracting from the cavities that appear to host end segments. The persistence length of DNA is about 50 nm, so hernias would be expected to form readily in the interconnecting holes (*25*). We tentatively ascribe the dynamics for this largest DNA to the beginnings of a crossover from entropic barriers transport to reptation.

Macromolecular diffusion in constrained environments has important technological and scientific ramifications. Most macromolecular separation techniques rely on the selective penetration and/or diffusion of macromolecules within gels and other media of ill-defined pore structure. In this context, switching from disordered to patterned media promises to improve both speed and resolution (*26–29*). Success as a separation medium hinges on the proper choice of pattern chemistry, feature size, dielectric mismatch, and surface charge. Weighed against its most prominent competitor, lithography, one can identify several advantages for colloidal templating—broad choice of pattern chemistry, reduced dielectric mismatch, and straightforward elimination of surface charge. On the other hand, the number of pattern geometries possible through colloidal templating remains limited (*30*).

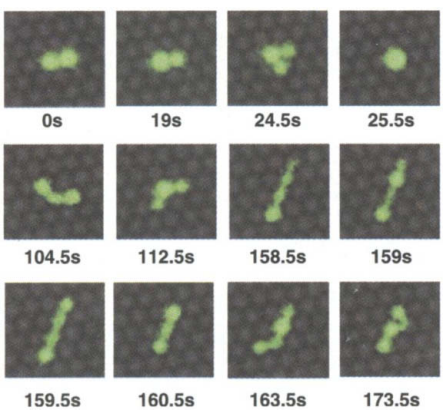

Fig. 5. A sampling at various times of configurations observed for a single 48.5-kbp DNA. The diffusing molecule has been recentered in each image.

References and Notes

1. T. W. Houseal, C. Bustamante, R. F. Stump, M. F. Maestre, *Biophys. J.* **56**, 507 (1989).
2. M. Matsumoto *et al.*, *J. Polym. Sci. B Polym. Phys.* **30**, 779 (1992).
3. J. Käs, H. Strey, E. Sackmann, *Nature* **368**, 226 (1994).
4. T. T. Perkins, D. E. Smith, S. Chu, *Science* **264**, 819 (1994).
5. D. L. Smisek, D. A. Hoagland, *Science* **248**, 1221 (1990).
6. G. W. Slater, P. Mayer, G. Drouin, *Methods Enzymol.* **270**, 272 (1996).
7. A. G. Ogston, *Trans. Faraday Soc.* **54**, 1754 (1958).
8. S. W. Turner, M. Cabodi, H. G. Craighead, *Phys. Rev. Lett.* **88**, 128103 (2002).
9. M. Muthukumar, A. Baumgärtner, *Macromolecules* **22**, 1937 (1989).
10. ———, *Macromolecules* **22**, 1941 (1989).
11. B. H. Zimm, O. Lumpkin, *Macromolecules* **26**, 226 (1993).
12. P. G. de Gennes, *J. Chem. Phys.* **55**, 572 (1971).
13. M. Doi, S. F. Edwards, *J. Chem. Soc. Faraday Trans. II* **74**, 1789 (1978).
14. T. P. Lodge, N. A. Rotstein, S. Prager, *Adv. Chem. Phys.* **79**, 1 (1990).
15. G. Guillot, L. Léger, F. Rondelez, *Macromolecules* **18**, 2531 (1985).
16. L. Masaro, X. X. Zhu, *Prog. Polym. Sci.* **24**, 731 (1999).
17. S. H. Park, Y. Xia, *Chem. Mater.* **10**, 1745 (1998).
18. P. Jiang, K. S. Hwang, D. M. Mittleman, J. F. Bertone, V. L. Colvin, *J. Am. Chem. Soc.* **121**, 11630 (1999).
19. L. Liu, P. Li, S. A. Asher, *Nature* **397**, 141 (1999).
20. D. E. Smith, T. T. Perkins, S. Chu, *Macromolecules* **29**, 1372 (1996).
21. J. W. Haus, K. W. Kehr, *Phys. Rep.* **150**, 263 (1987).
22. A. Einstein, *Ann. Phys.* **17**, 549 (1905).
23. ———, *Z. Electrochem. Angew. Phys. Chem.* **14**, 235 (1908).
24. P.-G. de Gennes, *Scaling Concepts in Polymer Physics* (Cornell Univ. Press, Ithaca, NY, 1979), pp. 193–197.
25. B. Åkerman, *Phys. Rev. E* **54**, 6686 (1996).
26. W. D. Volkmuth, R. H. Austin, *Nature* **358**, 600 (1992).
27. J. Han, S. W. Turner, H. G. Craighead, *Phys. Rev. Lett.* **83**, 1688 (1999).
28. C.-F. Chou *et al.*, *Proc. Natl. Acad. Sci. U.S.A.* **96**, 13762 (1999).
29. L. Meistermann, B. Tinland, *Phys. Rev. E* **52**, 4014 (2000).
30. K. P. Velikov, C. G. Christova, R. P. A. Dullens, A. v. Blaaderen, *Science* **296**, 106 (2002).
31. Support from the University of Massachusetts Material Research Science and Engineering Center. Engaging discussions of diffusion with M. Muthukumar are also acknowledged.

Supporting Online Material

www.sciencemag.org/cgi/content/full/297/5583/987/DC1

Movies S1 and S2

25 April 2002; accepted 5 July 2002

Formation of Immiscible Alloy Powders with Egg-Type Microstructure

C. P. Wang, X. J. Liu, I. Ohnuma, R. Kainuma,* K. Ishida

The egg-type core microstructure where one alloy encases another has previously been obtained during experiments in space. Working with copper-iron base alloys prepared by conventional gas atomization, we were able to obtain this microstructure under gravity conditions. The minor liquid phase always formed the core of the egg, and it sometimes also formed a shell layer. The origin of the formation of this core microstructure can be explained by Marangoni motion on the basis of the temperature dependence of the interfacial energy, which shows that this type of powder can be formed even if the cooling rate is very high.

Alloys immiscible in the liquid-phase region are characterized by a layer structure similar to that of the observed separation between oil and water, and thus they have been considered to be of no use for technical applications (*1*). Much effort has thus been made to obtain a finely dispersed distribution of both liquid phases (*2–5*). One of the most interesting trials was an experiment in space under microgravity conditions (*3*, *4*). For Al-In alloys, instead of a uniformly dispersed structure, an unexpected core microstructure was observed consisting of two layers with the Al-rich phase at the core of the sample (*3*). This fact suggests that it is difficult to obtain a finely dispersed microstructure, even without the influence of gravity.

In the present study, hypermonotectic Cu-Fe base alloys, in which the difference of density (ρ_{Fe} = 6.7 g/cm^3 and ρ_{Cu} = 7.5

Department of Materials Science, Graduate School of Engineering, Tohoku University, Aoba-yama 02, Sendai 980-8579, Japan.

*To whom correspondence should be addressed. E-mail: kainuma@material.tohoku.ac.jp

g/cm^3 at 1800 K) between immiscible liquid phases is relatively small in comparison with that in the Al-In system, were investigated. Two samples of powder with the composition of Cu-31.4Fe-3Si-0.6C (weight %) and Cu-51.4Fe-3Si-0.6C (weight %) were prepared, where the alloy compositions were designed to fall into the stable miscibility gap in the liquid state. The vertical section (Fe-3 weight % Si)-(Cu-3 weight % Si) of the phase diagram calculated with the thermodynamic parameters assessed by Wang and others (*6*), where the effect of carbon is neglected, is shown in Fig. 1. The volume fractions of the two liquid phases for Cu-31.4Fe-3Si (weight %) and Cu-51.4Fe-3Si (weight %) alloys are also shown in Fig. 1, B and C, respectively. The volume fractions of minor and major liquid phases are ~40 and 60%, respectively, for both alloys. These alloys were melted by high-frequency induction. Powders of 30 to 250 μm in diameter were obtained with conventional nitrogen gas atomization under an argon atmosphere, where the temperature of the melt before atomization was ~1800 to 2130 K and the gas pressure for atomizing was ~1.5 to 5 MPa. The cooling rate was 10^3 to 10^4 °C/s, depending on the size of the powder.

A typical cross-section microstructure of the Cu-rich [Cu-31.4Fe-3Si-0.6C (weight %)] atomized powder is shown in Fig. 2A. More than 70% of the powder shows a two-layer core microstructure composed of an Fe core and Cu periphery, which is similar to that observed in the Al-In alloys space experiments (*3*). The Fe core is located almost at the center of the sample. The rest of the powder exhibited a multicore structure, as shown in Fig. 2B. In the present study, we observed a reversal of the core and periphery phases. A typical microstructure of the Fe-rich [Cu-51.4Fe-3Si-0.6C (weight %)] powder with a diameter of less than ~50 μm is shown in Fig. 2C. The powder has a triple-layer core structure mainly consisting of a Cu core, an Fe periphery, and a thin Cu surface layer. From the examination of many alloys, it can be concluded that the minor volume phase always occupies the core part; that is, the Fe and Cu core structures are observed in the Cu- and Fe-rich alloys, respectively. This means that the minor phase droplets that appear in the major liquid phase during cooling must have rapidly assembled at the center of the powder against the temperature gradient illustrated in Fig. 2D. The existence of a multicore structure, as shown in Fig. 2B, where unification of the Fe droplets occurs near the center of the powder, supports this conclusion.

Young and others (*7*) and Ratke and others (*5*, *8*) reported that when there is an interfacial tension gradient between a spherical droplet and a liquid matrix, the droplets move toward the region with lower interfacial energy because of Marangoni motion (*9*). Because the viscous resistance from the matrix is in proportion to its velocity, the droplet attains uniform motion. The velocity of the droplet in such a steady state is given by

$$v_m \approx \frac{-2r}{3(3\mu_d + 2\mu_m)} \cdot \frac{\partial \sigma}{\partial T} \cdot \frac{\partial T}{\partial x} \quad (1)$$

where r is the radius of the droplet; μ_d and μ_m are the viscosities of the droplet and matrix liquid phases, respectively; σ is the interfacial energy; and x is the distance (*7*, *8*).

Therefore, interfacial energy between the two liquid phases must play a key role in the formation of the core microstructure. The interfacial energy between the two liquid phases in the A-B binary system is approximately proportional to the square of the concentration difference between them (*2*, *10*, *11*)

$$\sigma^{L1/L2} \approx \frac{N^* z^*}{N_0 z} \cdot L^L_{AB} \cdot (C^{L2}_B - C^{L1}_B)^2 \quad (2)$$

where N_0 is Avogadro's number, N^* is the number of front atoms per unit area of the interface, z is the coordination number, z^* is the number of cross bonds per front atom, L^L_{AB} is the interaction energy between A and B atoms, and $(C^{L2}_{Cu} - C^{L1}_{Cu})$ corresponds to the miscibility gap in the liquid phase. Simplifying the discussion, the interfacial energy between the Cu- and Fe-rich liquid phases is evaluated with the metastable miscibility gap in the Cu-Fe binary system. The values of L^L_{FeCu} and $(C^{L2}_{Cu} - C^{L1}_{Cu})$ are taken from the thermodynamic assessment (*12*), as shown in Fig. 3A. With the assumptions that $z = 12$, $z^* = 3$, and $N^* = 1.7 \times 10^{-9}$ m^{-2} (*11*), the interfacial energy $\sigma^{Cu/Fe}$ can be estimated as shown in Fig. 3B. The interfacial energy increases considerably with decreasing temperature because of the large temperature dependence of $(C^{L2}_{Cu} - C^{L1}_{Cu})$. This suggests that if there is a temperature gradient in the droplet, as illustrated in Fig. 2D, an interfacial tension gradient should also exist.

In estimating the contribution of the interfacial energy gradient driving the droplet, it

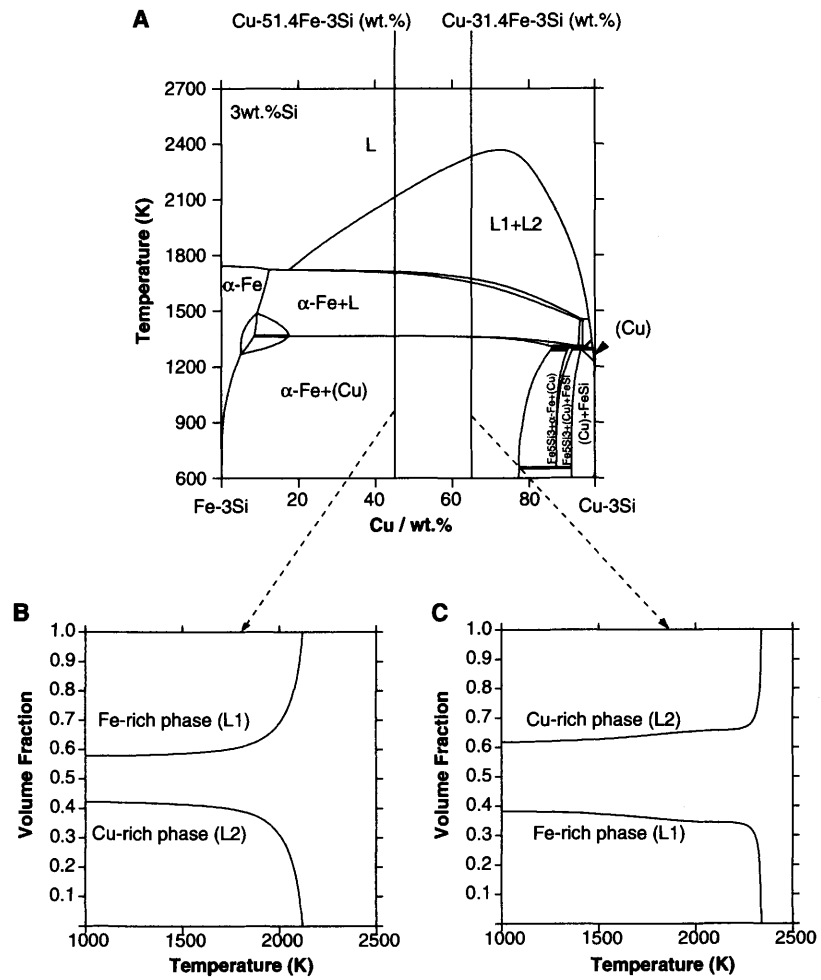

Fig. 1. Calculated (**A**) vertical section diagram (Fe-3weight %Si)-(Cu-3weight %Si) quasi-binary system and (**B** and **C**) the volume fraction of two liquid phases with the Cu-51.4Fe-3Si (weight %) and Cu-31.4Fe-3Si (weight %) alloys, respectively.

may be useful to examine the gravity effect described by Stokes equation (*8*)

$$v_s \approx \frac{2g\Delta\rho r^2}{3\mu_m} \cdot \frac{\mu_d + \mu_m}{3\mu_d + 2\mu_m} \quad (3)$$

where g (= 9.8 m/s^2) is the gravity coefficient and $\Delta\rho$ (< $\rho_{Cu} - \rho_{Fe}$ = 0.8 g/cm^3 at 1800 K) is the difference of density between the droplet and matrix phases. For example, with an Fe droplet of r = 5 μm existing in liquid Cu with temperature gradient $\partial T/\partial x$ = 1000 K/mm at T = 1550 K, v_m is ~55 mm/s. This is ~ 1.8 × 10^4 times the value of v_s (= 3.0 × 10^{-6} m/s) because of the gravity (buoyancy) effect, where $\partial\sigma/\partial T$ was evaluated by using the relation shown in Fig. 3B and the values of μ_d and μ_m were estimated from the method developed by Seetharaman and Sichen (*13*). This was confirmed by a similar calculation in the Al-In system. In the Al-In system, where there is a large difference of density between immiscible liquid phases, v_m at 973 K is still ~10^4 times as fast as v_s. These results suggest that it is Marangoni motion that causes the droplets to rapidly migrate to the center possessing the highest temperature. Thus, the core microstructure is formed during cooling, not only under microgravity conditions, but also under normal gravity conditions on Earth.

The reason why the Fe-rich powders show the triple-layer core structure consisting of mainly Cu core, Fe periphery, and a thin Cu surface layer, as shown in Fig. 2C, is not clear at present. However, the free-surface segregation of liquid Cu, with its surface energy lower than that of liquid Fe, and the rotation of the drops induced by the extremely rapid gas blow in the atomization process are probably connected to the formation of this thin Cu surface layer.

Because of technological interests and applications for egg-type powders, two examples of potential use are discussed. Powder compacts with Fe-Cu and Fe-Cu-C bases are widely used for automotive, electric, and industrial machinery, and they are fabricated by liquid-phase sintering of mixtures of Fe, C (graphite), and Cu powders, but there are problems with dimensional variations caused by the swelling of the C (graphite) and Cu powders (*14*). Thus, the development of a segregation-free Fe powder is expected to improve dimensional accuracy.

A second example is the development of a solder ball for modern electronics packaging technology. A solder ball is mainly used for the input/output terminal of the ball grid array (BGA) package. Compared to more conventional packages, the BGA package has the advantage of having higher input/output terminal density, a smaller footprint, and higher reliability (*15*). Recently, Cu core solders plated with a Pb-Sn eutectic alloy for BGA joints have been developed and used (*16*), where the Cu core solder ball shows both higher strength and high electronic conductivity in the core and a low melting point in the periphery. We show a promising BGA ball consisting of a core with a Cu base and a Pb-free low melting solder periphery. A powder of 24Cu-16Sn-60Bi (weight %) was prepared, in which a stable liquid miscibility gap appeared as predicted by the thermodynamic database for micro–solder alloys (*17*). The microstructure of this alloy powder is

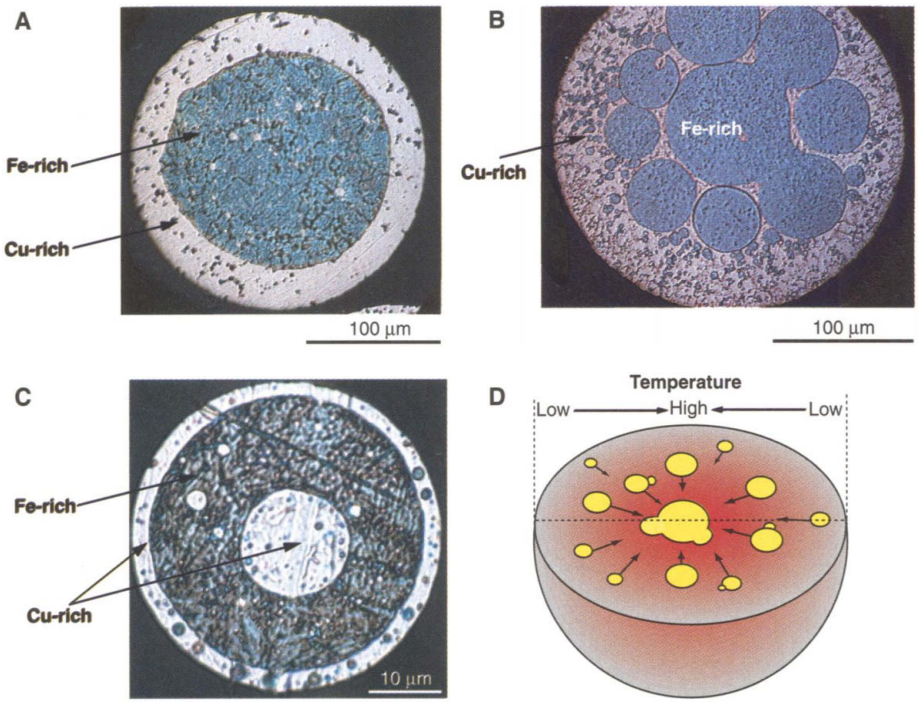

Fig. 2. (**A** and **B**) Microstructure of the Cu-31.4Fe-3Si-0.6C (weight %) alloy powders. (**C**) Microstructure of the Cu-51.4Fe-3Si-0.6C (weight %) alloy powder. (**D**) Schematic illustration demonstrating the microstructural evolution in the powder.

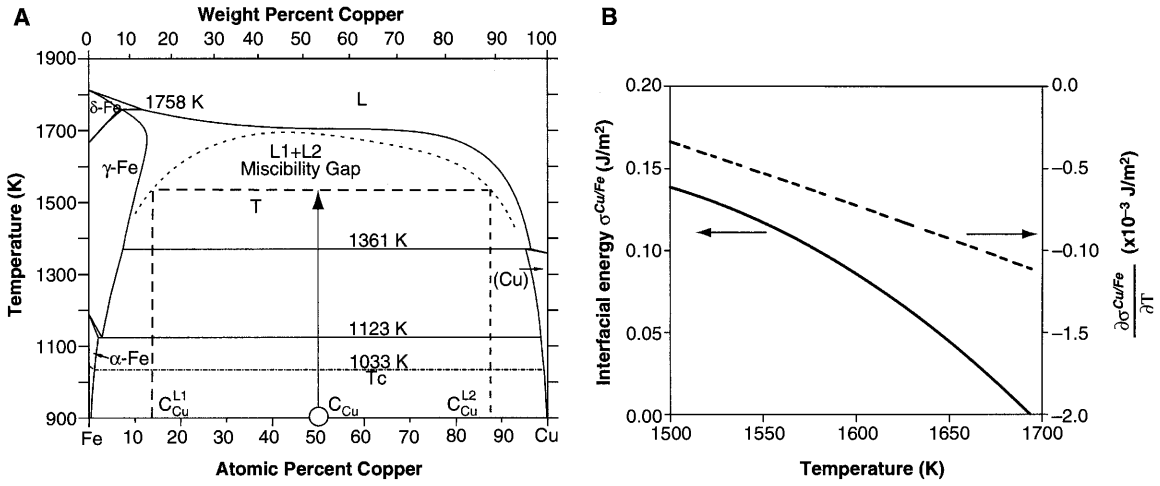

Fig. 3. (**A**) Fe-Cu experimental phase diagram with the metastable phase equilibrium between the Cu- and Fe-rich liquid phases in the Fe-Cu binary system obtained by thermodynamic calculation. (**B**) Interfacial energy and its differential between two liquid phases of the 50Cu-50Fe (weight %) alloy obtained by Eq. 1.

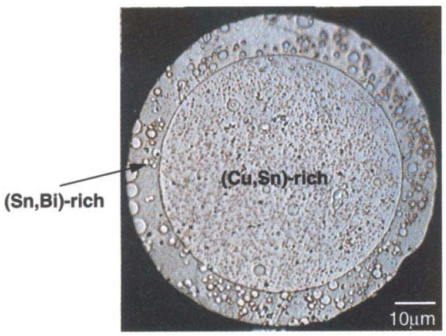

Fig. 4. Microstructure of the 24Cu-16Sn-60Bi (weight %) alloy powder.

shown in Fig. 4, indicating the egg-type structure of Cu-Sn–rich core with a Sn-Bi–rich periphery. The commercial size of a Cu core ball plated with Pb-Sn eutectic solder is ~700 μm, but a size of <100 μm is required for the chip-scale package, which is very difficult to produce by the conventional plating method. As shown in Fig. 4, the size of egg-type powder is ~80 μm.

The egg-type powder can be obtained in many alloy systems that possess a liquid miscibility gap. This simplified fabrication method may open up new applications for these alloy materials.

References and Notes

1. B. Predel, in *Thermodynamics of Alloy Formation*, Y. A. Chang and F. Sommer, Eds. (Minerals, Metals and Materials Society, Warrendale, PA, 1997), pp. 1–19.
2. L. Ratke, S. Diefenbach, *Mater. Sci. Eng.* **R15**, 263 (1995).
3. H. Ahlborn, K. Löhberg, in *17th Aerospace Sciences Meeting* (American Institute of Aeronautics and Astronautics, New York, 1979), pp. 3–7, paper 79-0172.
4. B. Predel, L. Ratke, H. Fredriksson, in *Fluid Sciences and Materials Science in Space: A European Perspective*, H. U. Walter, Ed. (Springer-Verlag, New York, 1987), pp. 517–565.
5. B. Prinz, A. Romero, L. Ratke, *J. Mater. Sci.* **30**, 4715 (1995).
6. C. P. Wang, X. J. Liu, I. Ohnuma, R. Kainuma, K. Ishida, *J. Phase Equilibria* **23**, 236 (2002).
7. N. O. Young, J. S. Goldstein, M. J. Block, *J. Fluid Mech.* **6**, 350 (1959).
8. L. Ratke, P. W. Voorhees, in *Growth and Coarsening* (Springer-Verlag, New York, 2002), pp. 239–249.
9. C. Marangoni, *Ann. Phys. Chem.* **143**, 337 (1871).
10. R. Becker, *Ann. Phys.* **32**, 128 (1938).
11. T. Nishizawa, I. Ohnuma, K. Ishida, *J. Phase Equilibria* **22**, 269 (2001).
12. Q. Chen, Z. P. Jin, *Metall. Mater. Trans. A* **26A**, 417 (1995).
13. S. Seetharaman, D. Sichen, *Metall. Mater. Trans. B* **25B**, 589 (1994).
14. S. J. Jamil, G. A. Chadwick, *Powder Metall.* **28**, 65 (1985).
15. E. Bradley, K. Banerji, *IEEE Trans. Components Packag. Manuf. Technol.* **B19**, 320 (1996).
16. S. Kiyono, K. Uenishi, K. Kobayashi, I. Shohji, M. Yamamoto, *J. Jpn. Inst. Electron. Packag.* **2**, 298 (1999).
17. I. Ohnuma, X. J. Liu, H. Ohtani, K. Ishida, *J. Electron. Mater.* **28**, 1163 (1999).
18. We thank Daido Steel Company for preparing the powders. Partially supported by a Grant-in-Aid for the Development of Innovative Technology.

18 April 2002; accepted 3 July 2002

Dipole Moments of Highly Vibrationally Excited Water

Andrea Callegari,[1] Patrice Theulé,[1] John S. Muenter,[2] Roman N. Tolchenov,[3] Nikalai F. Zobov,[3]* Oleg L. Polyansky,[3]* Jonathan Tennyson,[3] Thomas R. Rizzo[4]†

The intensity of water absorption in the region of the solar spectrum plays a dominant role in atmospheric energy balance and hence strongly influences climate. Significant controversy exists over how to model this absorption accurately. We report dipole moment measurements of highly vibrationally excited water, which provide stringent tests of intensities determined by other means. Our measurements and accompanying calculations suggest that the best currently available potential and dipole surfaces do not accurately model intensities in the optical spectrum of water.

The absorption of solar energy by molecules in the Earth's atmosphere and the subsequent energy transfer processes are of enormous importance in understanding global climatology. Despite the immense amount of experimental and theoretical work incorporated into atmospheric models, as much as 30% of solar radiant flux is not accounted for (*1–4*). Water is the dominant absorber in the Earth's atmosphere and plays a central role in climate evolution. However, this role is complicated and difficult to quantify, and there is substantial controversy over how well water absorption is modeled (*5–8*). Much of the controversy arises from the near-infrared (near-IR), visible, and near-ultraviolet (near-UV) portions of the spectrum, where water exhibits large numbers of weak spectroscopic transitions. These features occur at the peak of the solar spectrum and contribute a significant fraction of the total solar energy deposited in the atmosphere (*9*). Because the small intensities of the individual absorptions are difficult to measure accurately, theoretical calculations of water absorption profiles in these spectral regions can improve atmospheric models. However, the accuracy of these calculations must be independently confirmed for this approach to gain widespread acceptance. A number of other fields would also benefit from a better understanding of the water absorption spectrum, including the study of sunspots (*10*), cool star evolution (*11*), and rocket exhausts (*12*), as well as other disciplines in which water occurs in extreme environments.

The absorption spectrum of water, from the far-IR to the near-UV, is controlled by its electric dipole moment and the changes of this moment with vibrational motions. Molecular vibrations are specified by the potential energy surface (PES), which provides the total energy as an analytic function of internal coordinates used to describe molecular geometries. Similarly, the first moment of the charge distribution is given by the dipole moment surface (DMS). High-quality potential and dipole surfaces are both needed for the calculation of spectral intensities. Techniques for combining ab initio computations and experimental spectra to produce potential energy surfaces are well developed, and accurate potentials exist for water (*13, 14*), including those that go beyond the Born-Oppenheimer approximation (*15*).

The situation is less advanced for dipole moment surfaces. Ab initio calculations of dipole moments converge differently from those of energies and hence do not obey the variational principle. Thus, calculations that give comparable energies can produce quite different moments (*16–18*). Even when high-quality dipole moment calculations exist for a broad range of configurations, the choice of how to best parameterize the DMS is not trivial (*19*). Empirical DMSs rely on absolute spectroscopic intensity measurements, which are notoriously difficult to carry out with high accuracy. Moreover, it is surprisingly difficult to prepare simulated atmospheric samples containing accurately known densities of water (*20*). Even if one could measure accurate intensities, it is difficult to determine an accurate DMS from intensity measurements alone, as the inversion process would require an extremely accurate PES (*21*). Better modeling of the water absorption spectra, particularly the weak transitions in the visible and UV regions, requires new sources of accurate dipole moment data that can test and refine both ab initio and empirical DMSs. Perma-

[1]Laboratoire de chimie physique moléculaire (LCPM), École Polytechnique Fédérale de Lausanne, 1015 Lausanne, Switzerland. [2]Department of Chemistry, University of Rochester, Rochester, NY 14627, USA. [3]Department of Physics and Astronomy, University College London, Gower Street, London WC1E 6BT, UK. [4]Laboratoire de chimie physique moléculaire (LCPM), École Polytechnique Fédérale de Lausanne, 1015 Lausanne, Switzerland.

*Permanent address: Institute of Applied Physics, Russian Academy of Sciences, Uljanov Street 46, Nizhinii Novgorod, Russia 603950.

†To whom correspondence should be addressed. E-mail: thomas.rizzo@epfl.ch